

DETECTION OF PLANETARY EMISSION FROM THE EXOPLANET TrES-2 USING *SPITZER*/IRAC

FRANCIS T. O'DONOVAN^{1,2}, DAVID CHARBONNEAU³, JOSEPH HARRINGTON⁴, N. MADHUSUDHAN⁵, SARA SEAGER⁶, DRAKE DEMING⁷, HEATHER A. KNUTSON³

Draft version December 31, 2009

ABSTRACT

We present here the results of our observations of TrES-2 using the Infrared Array Camera on *Spitzer*. We monitored this transiting system during two secondary eclipses, when the planetary emission is blocked by the star. The resulting decrease in flux is $0.127\% \pm 0.021\%$, $0.230\% \pm 0.024\%$, $0.199\% \pm 0.054\%$, and $0.359\% \pm 0.060\%$, at $3.6\text{ }\mu\text{m}$, $4.5\text{ }\mu\text{m}$, $5.8\text{ }\mu\text{m}$, and $8.0\text{ }\mu\text{m}$, respectively. We show that three of these flux contrasts are well fit by a black body spectrum with $T_{\text{eff}} = 1500\text{ K}$, as well as by a more detailed model spectrum of a planetary atmosphere. The observed planet-to-star flux ratios in all four IRAC channels can be explained by models with and without a thermal inversion in the atmosphere of TrES-2, although with different atmospheric chemistry. Based on the assumption of thermochemical equilibrium, the chemical composition of the inversion model seems more plausible, making it a more favorable scenario. TrES-2 also falls in the category of highly irradiated planets which have been theoretically predicted to exhibit thermal inversions. However, more observations at infrared and visible wavelengths would be needed to confirm a thermal inversion in this system. Furthermore, we find that the times of the secondary eclipses are consistent with previously published times of transit and the expectation from a circular orbit. This implies that TrES-2 most likely has a circular orbit, and thus does not obtain additional thermal energy from tidal dissipation of a non-zero orbital eccentricity, a proposed explanation for the large radius of this planet.

Subject headings: eclipses — infrared: stars — stars: individual (GSC 03549-02811) — techniques: photometric

1. INTRODUCTION

There has been a recent dramatic increase in the number of extrasolar planets within 300 pc whose structures and atmospheric compositions can be probed using the *Spitzer Space Telescope* (Werner et al. 2004). These are the nearby transiting exoplanets. By measuring with *Spitzer* the decrease in light as one of these planets passes behind its star in an event known as a secondary eclipse, we can estimate the flux emitted by the planet. Detection of this emission from planetary atmospheres is made possible by taking advantage of the enhanced contrast between stars and their planets in the infrared wavelengths observable with *Spitzer*. Combining several of these flux measurements allows us to characterize the shape of the planet's emission spectrum, which tells us about the properties of its dayside atmosphere. (For a discussion of extrasolar planetary atmospheres, see Charbonneau et al. 2007; Marley et al. 2007).

The planets HD 209458b and HD 189733b have been

¹ NASA Postdoctoral Program Fellow, Goddard Space Flight Center, 8800 Greenbelt Rd, Greenbelt MD 20771

² California Institute of Technology, 1200 E. California Blvd., Pasadena, CA 91125; ftod@caltech.edu

³ Harvard-Smithsonian Center for Astrophysics, 60 Garden St., Cambridge, MA 02138

⁴ Department of Physics, University of Central Florida, Orlando, FL 32816

⁵ Department of Physics, Massachusetts Institute of Technology, 77 Massachusetts Ave., Cambridge, MA 02139

⁶ Department of Earth, Atmospheric, and Planetary Sciences, Massachusetts Institute of Technology, 77 Massachusetts Ave., Cambridge, MA 02139

⁷ Planetary Systems Laboratory, NASA Goddard Space Flight Center, Mail Code 693, Greenbelt, MD 20771

the optimal choices for *Spitzer* studies of extrasolar planetary atmospheres, because of their early discovery and the relative brightness of their stellar hosts. We have detected infrared emission from these exoplanets, both photometrically (Deming et al. 2005, 2006; Knutson et al. 2007, 2008), and with low-resolution spectroscopy (Richardson et al. 2007; Grillmair et al. 2007; Swain et al. 2008; Charbonneau et al. 2008; Grillmair et al. 2008; Swain et al. 2008, 2009a,b). Another early success was the report by Charbonneau et al. (2005) of the measurement of infrared light from TrES-1. More recently, Harrington et al. (2007), Deming et al. (2007b), Demory et al. (2007), and Machalek et al. (2008) announced the results from *Spitzer* observations of the transiting exoplanets HD 149026b, GJ 436b, and XO-1b.

There has been a flurry of activity to reconcile atmospheric models with this limited number of infrared measurements. While several attempts have been made to explain the infrared observations (see, e.g., Barman et al. 2005; Burrows et al. 2005, 2007a; Fortney et al. 2005, 2006; Seager et al. 2005), the models are not entirely in agreement and no single model can explain every observation. Recently, Burrows et al. (2007b), Burrows et al. (2008), and Fortney et al. (2008) supplied a possible piece of the puzzle by proposing that the very highly irradiated hot Jupiters such as HD 209458b and TrES-2 (see Fig. 1 of Fortney et al. 2008) will exhibit water emission rather than the expected water absorption at the IRAC wavelengths, a result of a temperature inversion in their atmospheres. The large stellar insolation that TrES-2 experiences may permit the presence

of TiO and/or VO molecules in the hot planetary atmosphere that would condense in a cooler atmosphere. These opaque molecules would then cause the inversion. However, while this hypothesis can explain the emission features seen in the spectrum of HD 209458b (Burrows et al. 2007b; Knutson et al. 2008), it is incomplete. The relatively lower insolation experienced by the planet XO-1b is similar to that of TrES-1, and hence both atmospheres would be predicted to have water absorption features, as is indeed supported by the infrared observations of TrES-1 by Charbonneau et al. (2005). Nevertheless, Machalek et al. (2008) have shown that XO-1b displays the contrary, with evidence of water emission in its atmosphere. More recently, Fressin et al. (2009) did not find any evidence for the expected thermal inversion in the atmosphere of the highly irradiated planet TrES-3. Zahnle et al. (2009) have shown that sulfur photochemistry may also lead to the formation of inversions. In their models, this photochemistry is more or less temperature independent between 1200 K and 2000 K, and is also relatively insensitive to atmospheric metallicity.

Although over 400 extrasolar planets are known, it is only for these nearby transiting exoplanets that we can measure the planetary radii and true planetary masses precisely enough to provide useful constraints for theoretical models. There have been problems reconciling the observed planetary masses and radii with models (see Laughlin et al. 2005, Charbonneau et al. 2007, Liu et al. 2008, and Ibgui & Burrows 2009, for a review), namely that there are planets such as TrES-2 whose radii are larger than predicted by the standard models for an irradiated gas giant planet. Several explanations have been proposed for bloated planets like TrES-2, mainly related to some additional source of energy to combat planetary contraction. One such possible energy source is the tidal damping of a non-zero eccentricity (Bodenheimer et al. 2001, 2003): the planetary orbit of a hot Jupiter is expected to be circular, unless it is gravitationally affected by an unseen planetary companion (see, e.g., Rasio & Ford 1996). We can constrain the likelihood of a tidal damping energy source by measuring the timing of the secondary eclipse of a transiting hot Jupiter like TrES-2 and comparing these timings to predictions based on transit timings and the hypothesis of a circular planetary orbit (see, e.g., Deming et al. 2005).

The transiting hot Jupiter TrES-2 (O'Donovan et al. 2006) is one of the known hot Jupiters with a radius larger than expected from current models. The atmosphere of TrES-2 experiences similar levels of irradiation from its host star as the atmosphere of the likewise bloated planet HD 209458b, and hence we expect to find evidence of a thermal inversion for TrES-2, according to the predictions of Burrows et al. (2007b), Burrows et al. (2008), and Fortney et al. (2008). Here we present the first *Spitzer* observations of TrES-2 (§2). From our analysis (§3), we have detected thermal emission from the transiting planet. We found no evidence for timing offsets of the secondary eclipses, and deduce the possible presence of a thermal inversion in the atmosphere of TrES-2 (§4).

2. IRAC OBSERVATIONS OF TRES-2

We monitored TrES-2 using *Spitzer* during the time of two secondary eclipses, employing a different pair of the four bandpasses available on the In-

TABLE 1
TRES-2 SYSTEM PARAMETERS

Parameter	Value	Reference
P (d)	2.470621 ± 0.000017	a
T_c (HJD)	$2,453,957.63479 \pm 0.00038$	a
$b = a \cos i / R_\star$	0.8540 ± 0.0062	a
i ($^\circ$)	83.57 ± 0.14	a
R_p / R_\star	0.1253 ± 0.0010	a
T_s [3.6 μm /5.8 μm] (HJD)	$2,454,324.5220 \pm 0.0026$	b
T_s [4.5 μm /8.0 μm] (HJD)	$2,454,070.04805 \pm 0.00086$	b

^a Holman et al. (2007).

^b This work.

frared Array Camera (IRAC; Fazio et al. 2004) during each of the eclipses. We took care to position TrES-2 (2MASS J19071403+4918590: $J = 10.232$ mag, $J - K_s = 0.386$ mag) away from array regions impaired by bad pixels or scattered light. We also kept the corresponding IRAC stray light avoidance zones free of stars that are bright in the infrared. We observed a $5.2' \times 5.2'$ field of view (FOV) containing TrES-2 during two eclipses, using the Stellar Mode of the IRAC instrument. On UT 2006 November 30 (starting at HJD 2,454,069.956), we obtained 1073 images of this FOV at 4.5 μm and 8.0 μm with an effective integration time of 10.4 s for a total observing time of 3.9 hr. Our 3.6- μm and 5.8- μm observations of TrES-2 were taken on UT 2007 August 16. The observations began at HJD 2,454,324.436 and lasted 4.0 hr, during which we acquired 2130 and 1065 images in the respective channels (of effective exposure time 1.2s and 10.4s, respectively).

3. DERIVING AND MODELING LIGHT CURVES OF TRES-2

As part of the Spitzer Science Center pipeline for IRAC data (version S15.0.5 for the 2006 observations, version S16.1.0 for the 2007 observations), the images were corrected for dark current, flat-field variations, and certain detector nonlinearities. Each header of these Basic Calibrated Data (BCD) images contains the time and date of observation and the effective integration time. We used these to compute the Julian date corresponding to mid-exposure of each observation. In order to convert these dates to Heliocentric Julian dates, we calculated the corresponding light travel time between the Sun and *Spitzer* (ranging from 0.5 to 2.5 minutes), using NASA JPL's HORIZONS⁸ service. We then computed the orbital phases using an updated orbital period and transit epoch (see Table 1) derived from observations (Holman et al. 2007) made as part of the Transit Light Curve project.

Using the nearest integer pixel (x_0, y_0) as an initial estimate of the position of TrES-2 on the array, we computed the flux-weighted centroid (x, y) of TrES-2 in each BCD image. The intra-pixel position of TrES-2 is then $(x' = x - x_0, y' = y - y_0)$. We measured the flux from our target using circular apertures ranging from 2 to 10 pixels, and subtracted the background signal assessed in a sky annulus with inner and outer radii of 20 and 30 pixels, respectively. We normalized the fluxes for a given channel and aperture size by dividing each time series by the median of its values outside the times of eclipse.

⁸ <http://ssd.jpl.nasa.gov/?horizons>

We examined the variation of the residual scatter of the out-of-eclipse data, and found that an aperture radius of 3 pixels produced the smallest residual scatter for all four channels. Figure 1 shows the four light curves we obtained using this photometric aperture.

For each of the observed secondary eclipses, we created a model of the two IRAC light curves obtained during that eclipse. We first accounted for various detector effects known to be present in IRAC data. There is a known correlation between the IRAC 3.6- μm or 4.5- μm flux from a source and the intra-pixel position (x', y') on the detector (Reach et al. 2005; Charbonneau et al. 2005, 2008; Knutson et al. 2008): the sensitivity of an individual pixel varies depending on the location of the stellar point-spread function (PSF), with higher fluxes measured near the center of the pixel and lower fluxes near the edges. Figure 1 shows this effect in our TrES-2 data. Data from these two channels also demonstrate a linear trend with time (as previously observed by Knutson et al. 2009 in IRAC observations of TrES-4), with a positive trend at 3.6 μm and a negative slope at 4.5 μm . We removed these trends to obtain f_0 , the actual stellar flux:

$$f_0 = f / ([c_1 + c_2 x' + c_3 y' + c_4 (x')^2 + c_5 (y')^2] \times [1 + C dt]), \quad (1)$$

where f is the measured stellar flux, (x', y') is the intra-pixel position, dt is the amount of time from the first observation, and (c_{1-5}, C) are free parameters in our model. The 5.8- μm and 8.0- μm data (see Fig. 1) display the “ramp” associated with these IRAC channels first noticed by Charbonneau et al. (2005), and expanded upon by Harrington et al. (2007) (supplementary information). Both data sets showed an overall increase in flux with dt . For these two data sets, we removed this detector effect by including the following correction in the model:

$$f_0 = f / [d_1 + d_2 (\ln dt') + d_3 (\ln dt')^2], \quad (2)$$

where d_{1-3} are free parameters, and $dt' = dt + 0.02$ days. Here our substitution of dt' for dt is simply to avoid division by infinity. We then modeled simultaneously the two corrected time series using the eclipse light curve equation for a uniform source from Mandel & Agol (2002). We obtained the required system parameters (see Table 1) from Holman et al. (2007): the planetary orbital period, impact parameter, orbital inclination, and the radius ratio between the planet and the star. Based on this ephemeris, we calculated the predicted eclipse epoch (T_s ; see Table 1). The three free parameters for the eclipse model were the timing offset (Δt), the eclipse depth at the shorter wavelength (Δf_l), and the depth at the longer wavelength (Δf_h). The model of the two light curves therefore has 12 free parameters: $[c_1, c_2, c_3, c_4, c_5, C, d_1, d_2, d_3, \Delta t, \Delta f_l, \Delta f_h]$.

For a particular instance of this model, we compute the χ^2 measure of the goodness of fit to the two relevant data sets as follows. For each light curve, we compute an initial uncertainty for the normalized flux values as their standard deviation. We exclude 5- σ outliers in flux from further consideration. We then exclude large outliers in intra-pixel position ($\max[|x' - x'_m|, |y' - y'_m|] > 0.15$, where $[x'_m, y'_m]$ are the median intra-pixel values) on the detector. We compute the χ^2 of the two light curves

TABLE 2
BEST-FIT VALUES FOR FREE
PARAMETERS OF ECLIPSE MODELS

Parameter	Value
3.6 μm /5.8 μm	
χ^2	3164
N	3166
Δt (min)	1.8 ± 3.6
$\Delta f_l (= \Delta f_{3.6 \mu\text{m}})$	$0.127\% \pm 0.021\%$
$\Delta f_h (= \Delta f_{5.8 \mu\text{m}})$	$0.199\% \pm 0.054\%$
4.5 μm /8.0 μm	
χ^2	2117
N	2119
Δt (min)	0.7 ± 3.1
$\Delta f_l (= \Delta f_{4.5 \mu\text{m}})$	$0.230\% \pm 0.024\%$
$\Delta f_h (= \Delta f_{8.0 \mu\text{m}})$	$0.359\% \pm 0.060\%$

separately, and rescale each χ^2 to reflect the reduction of the number of data points by the above outlier exclusion. We then sum the resulting values to compute the χ^2 of the overall model.

To find an initial estimate of the best-fit parameters for each model of two light curves, we first used the AMOEBA algorithm (Press et al. 1992) to minimize the χ^2 of the fit. Using this initial estimate as a starting point, we applied the Markov Chain Monte Carlo method (see, e.g., Ford 2005; Winn et al. 2007), computing the χ^2 at each of the 10^6 steps of the chain. We then calculated the median of the 10^6 χ^2 values, and excluded from further analysis all the steps prior to the occurrence of the first value lower than this median. For the i th free parameter of our model, we derived the best-fit value p_i as the median of the remaining distribution of values for that parameter. We computed the (possibly unequal) lower ($\sigma_{-,i}$) and upper ($\sigma_{+,i}$) errors in this value such that the ranges $[p_i - \sigma_{-,i}, p_i]$ and $[p_i, p_i + \sigma_{+,i}]$ each contain 68%/2 of the values less than or greater than, respectively, the best-fit value. We computed the flux residuals after dividing out the best-fit model, and then derived an updated uncertainty as the new standard deviation of the residuals from the model. We again computed and rescaled the χ^2 of the two light curves separately, and then summed the resulting values to compute the χ^2 of the best-fit.

We tabulate for both pairs of channels the best-fit values for the free parameters of the eclipse models and the reduced χ^2 in Table 2. We have overplotted in Figure 1 the above corrective functions using the best-fit parameters we derived from the Markov chains. In Figure 2, we plot the corrected fluxes from TrES-2 at the four wavelengths, and overplot the best-fit eclipse models. In both figures, the error bar shown for each binned data point is the standard deviation of the flux values in that bin, divided by the square root of the number of points in the bin.

4. DISCUSSION AND CONCLUSIONS

From the best-fit values (see Table 2) for the timing offset of the two observed secondary eclipses, we see that their weighted average ($\Delta t = 1.2 \pm 2.3$ min) is consistent

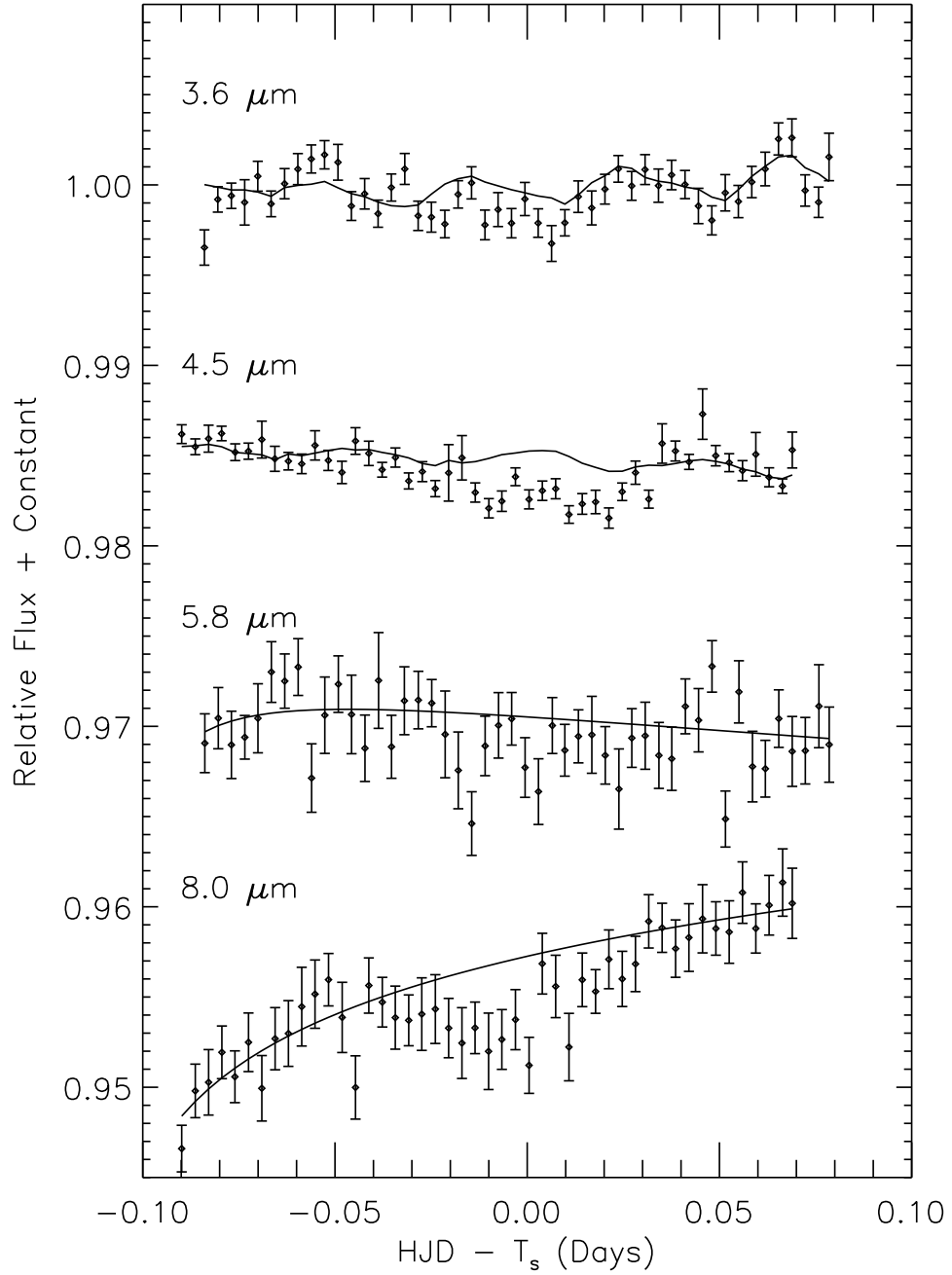


FIG. 1.— Relative fluxes from the system TrES-2 at $3.6\text{ }\mu\text{m}$, $4.5\text{ }\mu\text{m}$, $5.8\text{ }\mu\text{m}$, and $8.0\text{ }\mu\text{m}$ (with an arbitrary flux offset), binned and plotted vs. the time from the predicted center of secondary eclipse (T_s). Superimposed are our best-fit models (black lines) for known instrumental effects. The error bar shown for each binned data point is the standard deviation of the flux values in that bin, divided by the square root of the number of points in the bin.

with no offset from the predicted epochs for the eclipses. Note that we have not accounted for the light travel delay time (see Loeb 2005) of 37 s across the TrES-2 system, because of the relatively large size of the errors in these timing offsets compared to this delay time. An upper limit for the orbital eccentricity of a transiting planet can be computed from the timing offset Δt , using $e \cos \omega \simeq \pi \Delta t / 2 P$, where ω is the unknown longitude of periastron and P is the known orbital period (Charbonneau et al. 2005, Eq. 4). The 3σ upper limit for TrES-2 is therefore

0.0036, consistent with a negligible orbital eccentricity, unless $w \simeq 90^\circ$. Tidal damping of orbital eccentricity (Bodenheimer et al. 2001, 2003) is therefore unlikely to be a sizable contribution to the internal energy of this bloated exoplanet.

We now turn to a discussion of the TrES-2 planet-star contrasts. We first emphasize how well the data can be fit by a blackbody spectrum with no molecular band features. The black filled circles with error bars in Figure 3 show the *Spitzer* IRAC data points from

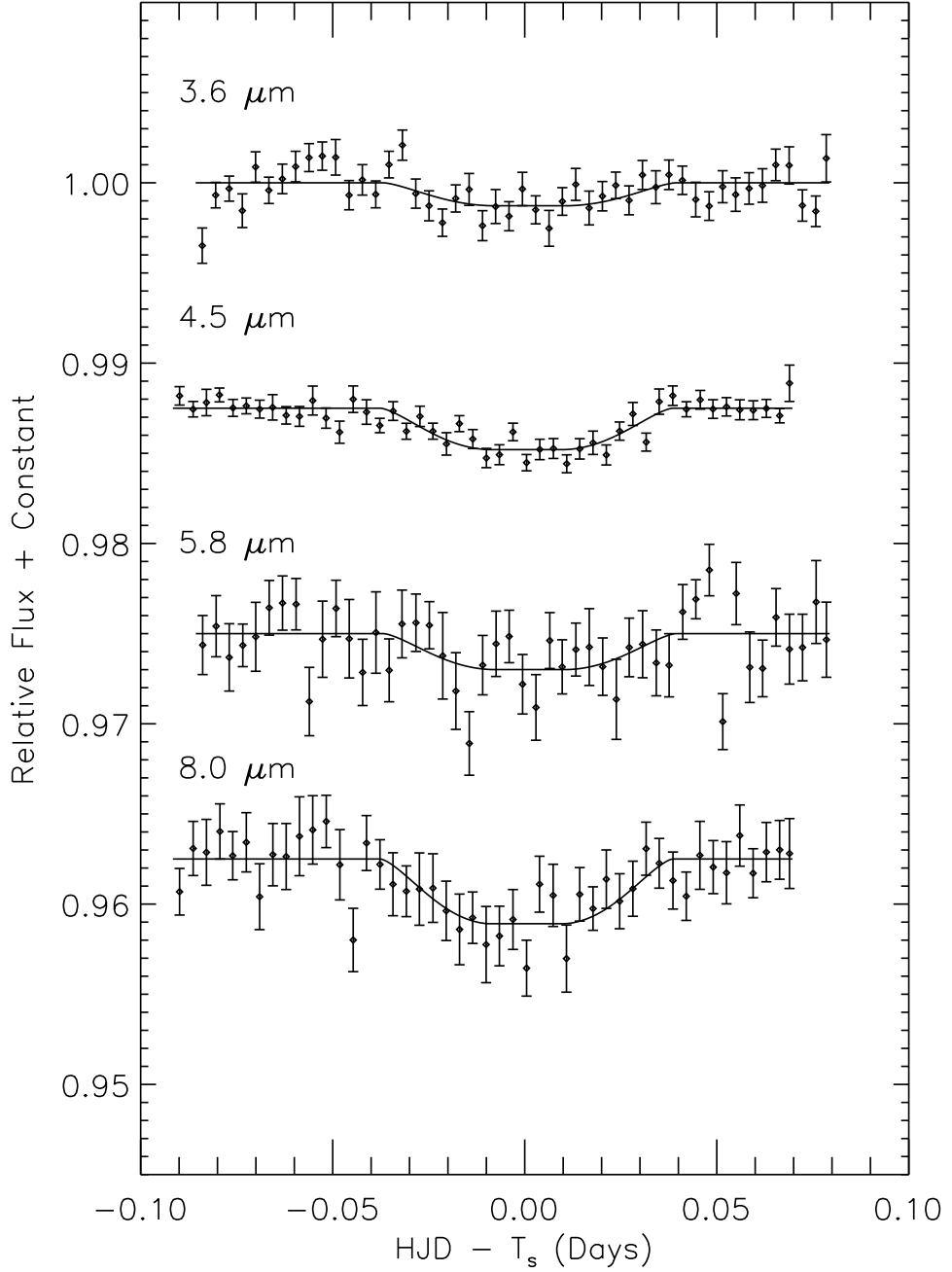


FIG. 2.— Same relative fluxes as Figure 1, except that here the fluxes have been corrected for the known detector effects. Overplotted are our best-fit models (black lines) of the secondary eclipses. The error bars are as in Figure 1.

this work. The *blue* dashed line is a 1500 K blackbody flux divided by the Kurucz stellar model with stellar parameters ($T_{\text{eff}} = 5750$ K, $Z = 0.0$, $\log(g) = 4.5$) closest to those ($T_{\text{eff}} = 5850 \pm 50$ K, $Z = -0.15 \pm 0.10$, $\log(g) = 4.4 \pm 0.1$) derived by Torres et al. (2008). It is clear that the blackbody fits all the data points reasonably well, given the large error bars. However, a blackbody spectrum is only a nominal guideline, since the actual planetary spectrum is influenced by the myriad contributions due to molecular band features, collision induced opacities, temperature gradients.

Model atmospheric spectra for TrES-2 are also shown in Figure 3. The red and green spectra show models with and without a thermal inversion on the planet day-side, respectively. The red and green circles (enclosed in black circles) show the corresponding model points obtained by integrating the spectra over the *Spitzer* IRAC bandpasses. The corresponding model thermal profiles are shown in Figure 4. The spectra were generated using the hot Jupiter atmosphere model developed in Madhusudhan & Seager (2009). We consider a cloudless atmosphere, and the molecular species are assumed to be

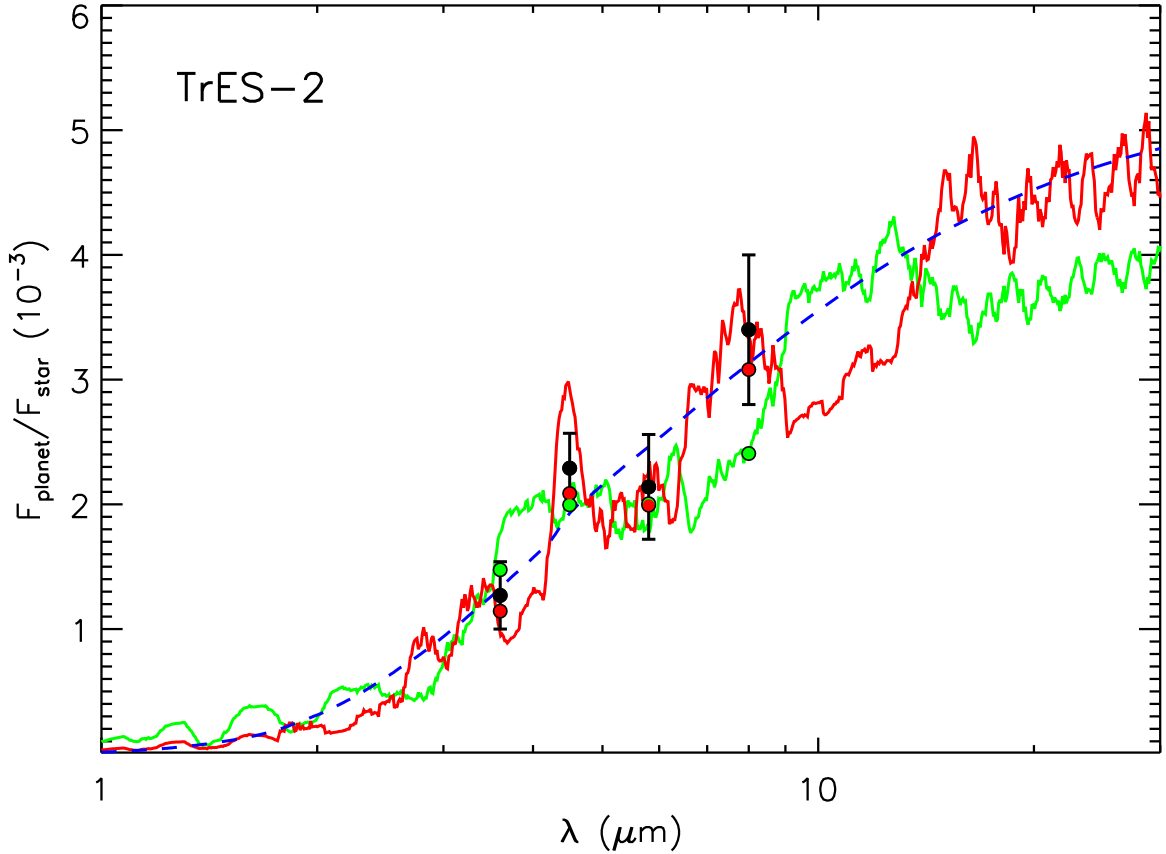


FIG. 3.— Contrast ratios (black filled circles) for TrES-2 at $3.6\mu\text{m}$, $5.8\mu\text{m}$ and $8.0\mu\text{m}$, which are consistent with a model (blue line) of a 1500 K black body planetary flux divided by a Kurucz model of the star TrES-2. Our additional observation at $4.5\mu\text{m}$ shows some evidence of excess emission at this wavelength. Also shown are the predictions (red and green circles) for these four fluxes from theoretical planet-star flux contrast models (red and green lines) computed for the star TrES-2 using the Madhusudhan & Seager (2009) code (see text). The red (green) spectrum corresponds to a model with (without) a thermal inversion on the planet dayside.

well mixed. The stellar spectrum was represented by the appropriate Kurucz model. The model spectrum without a thermal inversion has $T_{\text{eff}} = 1634\text{ K}$, and the model spectrum with a thermal inversion has $T_{\text{eff}} = 1459\text{ K}$. Both the models allow for extremely efficient day-night energy redistribution. At face value, we find that both the models fit the data almost equally well.

However, the two models require different molecular compositions, which helps us determine the more probable model. The model without a thermal inversion has uniform molecular mixing ratios of 10^{-4} for H_2O , 10^{-6} for CO , and 10^{-6} for CH_4 . While the mixing ratio of H_2O is plausible, the low mixing ratio of CO is surprising. In a hot atmosphere, with $T_{\text{eff}} = 1500\text{ K}$, CO is expected to be highly abundant. On the other hand, the model with a thermal inversion has uniform molecular mixing ratios of 10^{-4} for H_2O , 10^{-4} for CO , 5×10^{-5} for CH_4 , and 2×10^{-6} for CO_2 . These compositions show a relatively high abundance of CO , as expected in a hot Jupiter atmosphere like that of TrES-2. Based on these compositions, the presence of a thermal inversion seems like a more favorable scenario. Additionally, the requirement of 2×10^{-6} of CO_2 for the inversion model suggests an enhanced metallicity of $[M/H] \sim 0.7$ (Zahnle et al.

2009). However, a thorough exploration of the parameter space is needed to place constraints on the thermal inversion in conjunction with the molecular compositions (Madhusudhan & Seager 2010).

Thus we see some evidence that TrES-2 is part of the group of planets that display excess emission at wavelengths longer than $4\mu\text{m}$. The presence of a thermal inversion in the atmosphere of TrES-2 would support the theory of Fortney et al. (2008) and Burrows et al. (2008) that planets with substellar fluxes greater than or equal to approximately $10^9\text{ erg s}^{-1}\text{ cm}^{-2}$ should show evidence for a temperature inversion in their atmospheres.

Our theoretical models for the planetary flux from TrES-2 are currently constrained only at infrared wavelengths. Such an infrared signal appears to be relatively insensitive to cloud cover (Burrows et al. 2005). However, the amount of starlight reflected off the planetary atmosphere (at optical wavelengths) is highly dependent on the presence and size of upper-atmospheric condensates such as MgSiO_3 , Fe and Al_2O_3 (Marley et al. 1999; Green et al. 2003). Hence, a tighter constraint of atmospheric models for TrES-2 would be derived from the combination of measurements of the optical planetary flux from observations of secondary eclipses with the re-

sults from our infrared observations. Two likely sources for such observations of the optical flux from TrES-2 are the Kepler mission (Borucki et al. 1997) and the EPOXI mission (Deming et al. 2007a). Kepler has already demonstrated the ability to monitor the variation in thermal emission and reflected light from HAT-P-7 (Borucki et al. 2009). We eagerly await the comparison of our infrared observations with future optical observations from these two missions.

Although our observations of the atmospheric emission from TrES-2 at $3.6\text{ }\mu\text{m}$, $4.5\text{ }\mu\text{m}$, $5.8\text{ }\mu\text{m}$, and $8.0\text{ }\mu\text{m}$ provide limited spectral coverage, we have been able to deduce the probable presence of gaseous molecules with high opacities in the atmospheric that result in emission in the $4.5\text{ }\mu\text{m}$ band. The highly irradiated gas giant TrES-2 thus may provide additional evidence for the correlation between the occurrence of thermal inversion in the atmosphere of a planet and the level of stellar insolation experienced by the planet.

Our observations of two secondary eclipses by this ex-

oplanet occurred at the time predicted using the time of transit and the assumption of a circular orbit, within the errors. From this we conclude that the source of additional energy required to inflate the planetary radius to its bloated size is unlikely to be tidal heating caused by the circularization of an eccentric orbit.

This work is based on observations made with the Spitzer Space Telescope, which is operated by the Jet Propulsion Laboratory, California Institute of Technology under a contract with the National Aeronautics and Space Administration (NASA). This research was supported in part by NASA under grant NNG05GJ29G (issued through the Origins of Solar Systems Program), and also by an appointment to the NASA Postdoctoral Program at the Goddard Space Flight Center (administered by Oak Ridge Associated Universities through a contract with NASA).

Facilities: Spitzer (IRAC)

REFERENCES

- Barman, T. S., Hauschildt, P. H., & Allard, F. 2005, *ApJ*, 632, 1132
 Bodenheimer, P., Laughlin, G., & Lin, D. N. C. 2003, *ApJ*, 592, 555
 Bodenheimer, P., Lin, D. N. C., & Mardling, R. A. 2001, *ApJ*, 548, 466
 Borucki, W. J., et al. 2009, *Science*, 325, 709
 Borucki, W. J., Koch, D. G., Dunham, E. W., & Jenkins, J. M. 1997, in *ASP Conf. Ser.* 119: Planets Beyond the Solar System and the Next Generation of Space Missions, ed. D. Soderblom, 153
 Burrows, A., Budaj, J., & Hubeny, I. 2008, *ApJ*, 678, 1436
 Burrows, A., Hubeny, I., Budaj, J., & Hubbard, W. B. 2007a, *ApJ*, 661, 502
 Burrows, A., Hubeny, I., Budaj, J., Knutson, H. A., & Charbonneau, D. 2007b, *ApJ*, 668, L171
 Burrows, A., Hubeny, I., & Sudarsky, D. 2005, *ApJ*, 625, L135
 Charbonneau, D., et al. 2005, *ApJ*, 626, 523
 Charbonneau, D., Brown, T. M., Burrows, A., & Laughlin, G. 2007, in *Protostars and Planets V*, ed. B. Reipurth, D. Jewitt, & K. Keil (Tucson: University of Arizona Press), 701
 Charbonneau, D., Knutson, H. A., Barman, T., Allen, L. E., Mayor, M., Megeath, S. T., Queloz, D., & Udry, S. 2008, *ApJ*, 686, 1341
 Deming, D., et al. 2007a, in *Bulletin of the American Astronomical Society*, Vol. 38, *Bulletin of the American Astronomical Society*, 450
 Deming, D., Harrington, J., Laughlin, G., Seager, S., Navarro, S. B., Bowman, W. C., & Horning, K. 2007b, *ApJ*, 667, L199
 Deming, D., Harrington, J., Seager, S., & Richardson, L. J. 2006, *ApJ*, 644, 560
 Deming, D., Seager, S., Richardson, L. J., & Harrington, J. 2005, *Nature*, 434, 740
 Demory, B.-O., et al. 2007, *A&A*, 475, 1125
 Fazio, G. G., et al. 2004, *ApJS*, 154, 10
 Ford, E. B. 2005, *AJ*, 129, 1706
 Fortney, J. J., Cooper, C. S., Showman, A. P., Marley, M. S., & Freedman, R. S. 2006, *ApJ*, 652, 746
 Fortney, J. J., Lodders, K., Marley, M. S., & Freedman, R. S. 2008, *ApJ*, 678, 1419
 Fortney, J. J., Marley, M. S., Lodders, K., Saumon, D., & Freedman, R. 2005, *ApJ*, 627, L69
 Fressin, F., Knutson, H. A., Charbonneau, D., O'Donovan, F. T., Burrows, A., Deming, D., & Mandushev, G. 2009, *arxiv:0909.5221*
 Green, D., Matthews, J., Seager, S., & Kuschnig, R. 2003, *ApJ*, 597, 590
 Grillmair, C. J., et al. 2008, *Nature*, 456, 767
 Grillmair, C. J., Charbonneau, D., Burrows, A., Armus, L., Stauffer, J., Meadows, V., Van Cleve, J., & Levine, D. 2007, *ApJ*, 658, L115
 Harrington, J., Luszcz, S., Seager, S., Deming, D., & Richardson, L. J. 2007, *Nature*, 447, 691
 Holman, M. J., et al. 2007, *ApJ*, 664, 1185
 Ibgui, L., & Burrows, A. 2009, *ApJ*, 700, 1921
 Knutson, H. A., Charbonneau, D., Allen, L. E., Burrows, A., & Megeath, S. T. 2008, *ApJ*, 673, 526
 Knutson, H. A., et al. 2007, *Nature*, 447, 183
 Knutson, H. A., Charbonneau, D., Burrows, A., O'Donovan, F. T., & Mandushev, G. 2009, *ApJ*, 691, 866
 Laughlin, G., Wolf, A., Vanmunster, T., Bodenheimer, P., Fischer, D., Marcy, G., Butler, P., & Vogt, S. 2005, *ApJ*, 621, 1072
 Liu, X., Burrows, A., & Ibgui, L. 2008, *ApJ*, 687, 1191
 Loeb, A. 2005, *ApJ*, 623, L45
 Machalek, P., McCullough, P. R., Burke, C. J., Valenti, J. A., Burrows, A., & Hora, J. L. 2008, *ApJ*, 684, 1427
 Madhusudhan, N., & Seager, S. 2009, *ApJ*, 707, 24
 Madhusudhan, N., & Seager, S. 2010, *ApJ*, submitted
 Mandel, K., & Agol, E. 2002, *ApJ*, 580, L171
 Marley, M. S., Fortney, J., Seager, S., & Barman, T. 2007, in *Protostars and Planets V*, ed. B. Reipurth, D. Jewitt, & K. Keil (Tucson: University of Arizona Press), 733
 Marley, M. S., Gelino, C., Stephens, D., Lunine, J. I., & Freedman, R. 1999, *ApJ*, 513, 879
 O'Donovan, F. T., et al. 2006, *ApJ*, 651, L61
 Press, W. H., Teukolsky, S. A., Vetterling, W. T., & Flannery, B. P. 1992, *Numerical Recipes in C* (Cambridge: Cambridge University Press)
 Rasio, F. A., & Ford, E. B. 1996, *Science*, 274, 954
 Reach, W. T., et al. 2005, *PASP*, 117, 978
 Reipurth, B., Jewitt, D., & Keil, K., ed. 2007, *Protostars and Planets V* (Tucson: University of Arizona Press)
 Richardson, L. J., Deming, D., Horning, K., Seager, S., & Harrington, J. 2007, *Nature*, 445, 892
 Seager, S., Richardson, L. J., Hansen, B. M. S., Menou, K., Cho, J. Y.-K., & Deming, D. 2005, *ApJ*, 632, 1122
 Swain, M. R., Bouwman, J., Akeson, R. L., Lawler, S., & Beichman, C. A. 2008, *ApJ*, 674, 482
 Swain, M. R., et al. 2009a, *ApJ*, 704, 1616
 Swain, M. R., Vasisht, G., & Tinetti, G. 2008, *Nature*, 452, 329
 Swain, M. R., Vasisht, G., Tinetti, G., Bouwman, J., Chen, P., Yung, Y., Deming, D., & Deroo, P. 2009b, *ApJ*, 690, L114
 Torres, G., Winn, J. N., & Holman, M. J. 2008, *ApJ*, 677, 1324
 Werner, M. W., et al. 2004, *ApJS*, 154, 1
 Winn, J. N., Holman, M. J., & Fuentes, C. I. 2007, *AJ*, 133, 11
 Zahnle, K., Marley, M. S., Freedman, R. S., Lodders, K., & Fortney, J. J. 2009, *ApJ*, 701, L20

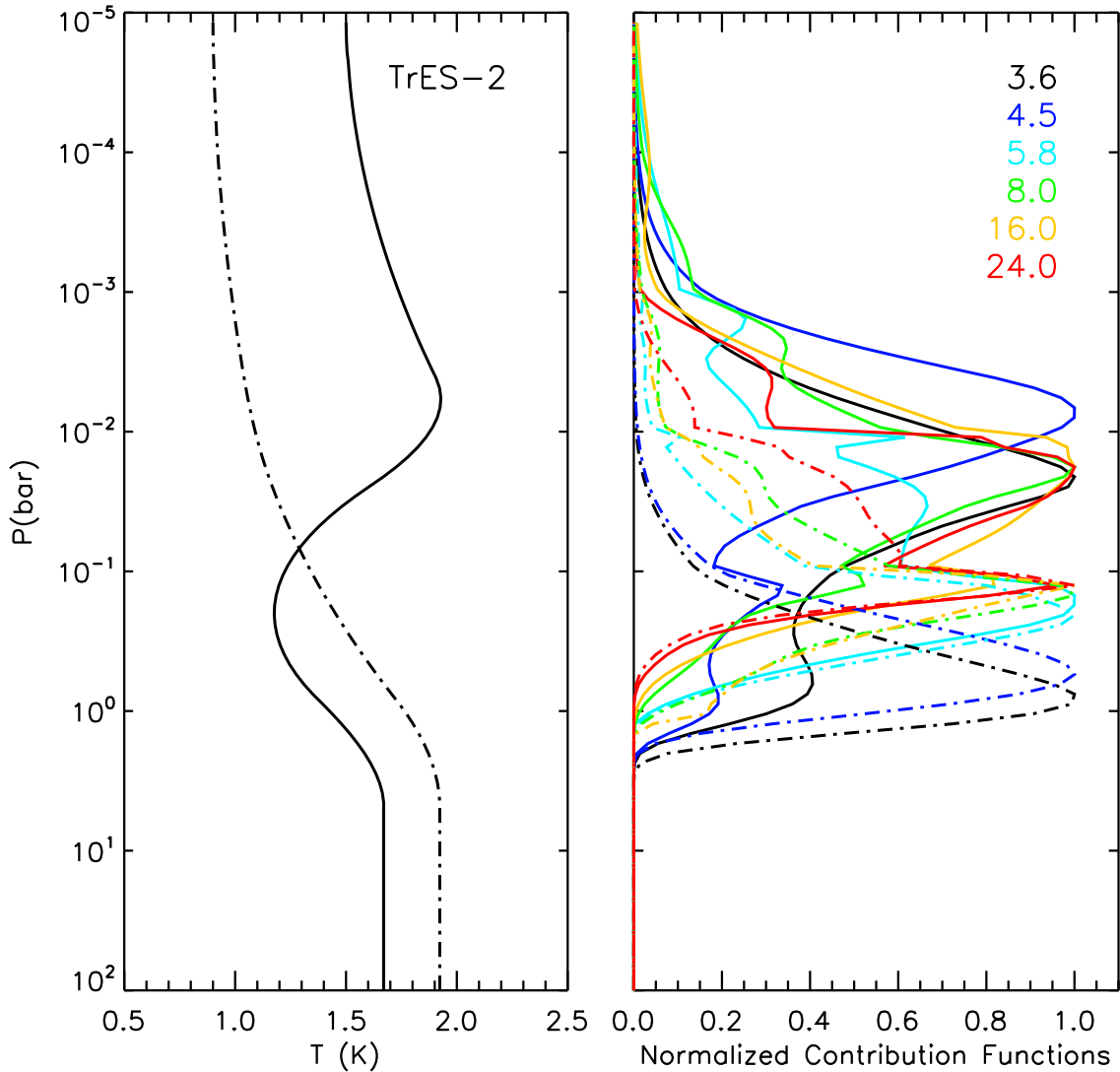


FIG. 4.— Pressure-Temperature profiles and contribution functions corresponding to the models shown in Figure 3. The left panel shows the two pressure temperature profiles (with and without a thermal inversion) corresponding to the two models reported in this work. The *solid* (*dash-dot*) curve shows the *P-T* profile with (without) a thermal inversion. Both the profiles lead to good fits to the observations, albeit with different molecular compositions. The *P-T* profiles were generated with the parametric prescription developed in Madhusudhan & Seager (2009). The thermal inversion in the *solid* profile lies between 0.20–0.01 bar, and spans temperatures between 1100–2000 K. The right panel shows the contribution functions in the six Spitzer photometric channels for each model. The legend shows the channel center wavelength in microns, and the curves are color-coded by the channel. The *solid* curves show the contribution functions for the inversion model, whereas the *dash-dot* curves show the contribution functions for the non-inversion model. All the contribution functions are normalized to unity.